Interdiffusion at electrochemical interfaces between yttria-stabilized zirconia and doped ceria

Alexander Schwiers[1,2], Christian Lenser[1], Olivier Guillon[1,2,3], Norbert H. Menzler[1,2]

[1] Forschungszentrum Jülich GmbH, Institute of Energy and Climate Research (IEK), Materials Synthesis and Processing (IEK-1)
Wilhelm-Johnen-Straße, 52428 Juelich/Germany
[2] RWTH Aachen University, Institute of Mineral Engineering (GHI), Aachen
[3] JARA-Energy, Juelich

Abstract

Integration of doped ceria into fuel electrode-supported solid oxide cells is challenging due to high sintering temperatures leading to undesirable interdiffusion between the layers.
We investigate the influence of the dopant in ceria $X_{0.1}Ce_{0.9}O_{1.95}$ (10XDC, X = Y, Gd or Sm) on the interdiffusion with yttria-stabilized zirconia (8YSZ). Powder mixtures of 8YSZ and 10XDC were sintered at temperatures between 1000–1400 °C to quantify the phase formation. Interdiffusion in layered systems sintered at 1400 °C was investigated by SEM. Symmetrical Ni-10XDC cells with an 8YSZ electrolyte were analyzed using impedance spectroscopy. Despite small differences in the interdiffusion behavior, different dopants do not lead to significant changes in the cell impedance.
Notably, the presence of NiO in the fuel electrode leads to enhanced interdiffusion kinetics of 10XDC with 8YSZ and the formation of porosity at the electrolyte interface. The detrimental influence of these microstructural changes on the electrode performance was investigated.

Graphical abstract

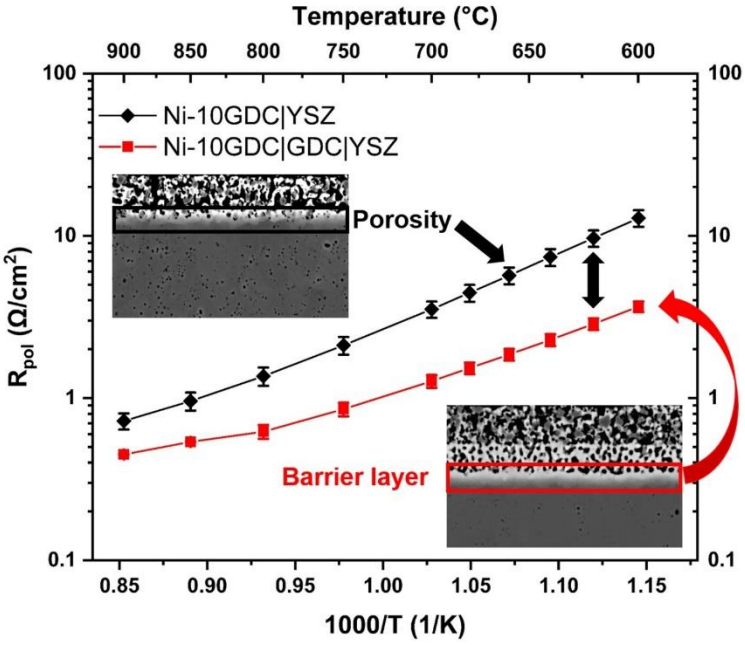

Keywords

Interdiffusion; Interfaces; Electrochemistry; Fuel cell materials; Doped ceria

1 Introduction

Fuel electrode-supported solid oxide fuel cells (FESC) show promising power densities for stationary applications due to their thin electrolyte. Furthermore, the thin electrolyte offers the possibility to lower the operation temperature and possibly enable applications beyond stationary power generation.
The material of choice for the electrolyte and the ion-conductor in the fuel electrode is 8-mol% yttria-stabilized zirconia ($Y_{0.148}Zr_{0.852}O_{1.926}$, 8YSZ) due to its compelling combination of stability, conductivity and material compatibility [1]. Doped ceria (often gadolinium doped ceria, $Gd_{0.1}Ce_{0.9}O_{1.95}$, 10GDC) is seen as a strong alternative for the fuel electrode due to the higher ionic conductivities in the intermediate temperature regime (500-700 °C) [2] as well as improved degradation tolerance towards products of internal reformation reactions if the fuel contains higher hydrocarbons (especially tars are concerning) and other contaminants like sulfur species (e.g. in biogas) [3-12].
Obtaining the desired microstructure in a FES-half cell (Substrate | fuel-electrode | electrolyte) requires high sintering temperatures, in the present case 1400 °C for 5 h [13]. Interdiffusion between different materials is substantial in this temperature regime. The substitution of 8YSZ as fuel electrode material by 10GDC leads to interdiffusion during the sintering process at the interface between fuel electrode and electrolyte materials [14, 15]. The consequences of the interdiffusion process are well documented on the air electrode side of an FESC [16-21] but less on the fuel electrode side. In a first attempt to replace the Ni-8YSZ fuel electrode in our state-of-the-art FESC with a Ni-10GDC fuel electrode the electrochemical performance of the cell was reduced, to an extend that cannot be simply explained by the formation of a mixed phase alone [22].
Therefore, we investigated the interdiffusion between doped ceria and cermets of NiO and doped ceria with 8YSZ and its influence on cell performance on the fuel side. The interdiffusion process leads to the formation of a mixed phase with reduced conductivity at the interface, and to the formation of Kirkendall voids due to the different interdiffusion coefficients of the respective cations. The main focus of prior works in the literature is on the mixed phase formation and its influence on conductivity [23-26]. Notably, on the air side of the cell, the formation of a mixed 8YSZ/10GDC phase has been shown to be the key factor to prevent the formation of $SrZrO_3$, which exhibits drastically lower conductivity. This study proposes that on the fuel side, the emerging porosity at the electrochemical active electrode/electrolyte interface shows a significant and detrimental influence too.
We also investigate whether the dopant in ceria can be chosen to mitigate the interdiffusion between doped ceria and 8YSZ. The size of the dopant might influence the diffusion of the respective cations in terms of lattice and grain boundary diffusion [27]. We investigate the influence of the dopant in ceria (XDC, X = Y, Gd, Sm) on the interdiffusion behavior with 8YSZ in powder mixtures by i) XRD analysis of the phase formation, ii) ionic conductivity measurements of the mixed phase, iii) determining the interdiffusion lengths by material contrast in layered systems using SEM and iv) the influence of interdiffusion on the impedance response of symmetrical cells by electrochemical impedance spectroscopy (EIS).
We observed that the presence of NiO in the fuel electrode enhances the interdiffusion of the respective cations and leads to the formation of Kirkendall voids and porosity at the Ni-10XDC-electrode/8YSZ-electrolyte interface. Such porosity is not formed in the absence of NiO. The influence of these microstructural changes is again investigated using EIS. Based on these results, we evaluate if the choice of an appropriate dopant can mitigate or reduce the negative

effects of interdiffusion at the interface between doped ceria and 8YSZ during FESC fabrication, or if additionally on the fuel side diffusion barrier layers need to be implemented.

2 Materials & Methods

Five commercially available raw powders were used: Yttria-stabilized zirconia $Y_{0.148}Zr_{0.852}O_{1.926}$ (8YSZ, Tosoh, Japan), gadolinia-doped ceria $Gd_{0.1}Ce_{0.9}O_{2-\delta}$ (10GDC, Fuelcellmaterials, USA) yttria-doped ceria $Y_{0.1}Ce_{0.9}O_{2-\delta}$ (10YDC, Cerpotech, Norway) and samaria-doped ceria $Sm_{0.1}Ce_{0.9}O_{2-\delta}$ (10SDC, Kceracell, Korea) and nickel oxide NiO (Vogler, The Netherlands).
Particle sizes have been measured in ethanol with a laser scattering particle size distribution analyser (Partica LA-950V2 by Retsch Technology). Beforehand, an ultrasonic treatment was used to break loose agglomerates.
The specific surface area was determined by nitrogen gas absorption (BET) with an Areameter (Jung Instruments Areamat).

2.1 Phase analysis of powder mixtures

For XRD analysis pellets containing 42 mol% of 8YSZ and 58 mol% of 10XDC were mixed and ball milled for 24 h in ethanol to ensure homogenization of the powders and to break agglomerates. The suspensions were dried, and the powder uniaxially pressed into pellets with a diameter of 20 mm and cold-isostatically pressed afterwards. The pellets were sintered at temperatures between 1000 °C and 1400 °C with an increment of 100 °C for 5 h. Subsequently, the surface of the pellets was ground and analysed with XRD using a Bruker D4 Endeavor X-Ray Diffractometer. The phase composition was analysed using a polynomial fit to determine the position of the diffraction lines, and a subsequent Rietveld refinement method to determine the phase composition. To determine the phase composition, it is necessary to get insight into the relationship between the lattice parameter and the stoichiometry of the material. Therefore, additional samples were prepared with different stoichiometries. The corresponding relationship between 8YSZ and 10XDC follows Vegard´s Law. The Vegard´s relationships are shown in detail in Figure S1 found in the SI.

2.2 Determination of interdiffusion lengths

To determine interdiffusion lengths in layered screen-printed systems, pre-suspensions were prepared containing 64.10 wt% of XDC, 33.34 wt% of terpineol, 2.56 wt% BYK P-104 dispersant and were mixed with grinding balls using a tumbling mixer for 24 h. Afterwards, a slurry was formed by adding 16 wt% of a transport agent (15 wt% ethyl cellulose [10cps] dissolved in 85 wt% terpineol) to the pre-suspension.
The layers were printed on dense, ~200 µm-thick 8YSZ substrates (Kerafol, Germany) using a semi-automatic screen printer (EKRA E-2). The mesh used leads to a layer of about ~ 5-8 µm after sintering at 1400 °C for 5 h (according to FES-half cell sintering conditions).
Scanning electron micrographs of polished cross-sections were recorded with a Zeiss EVO equipped with a back scattered electron detector.

2.3 Impedance analysis of symmetrical cells

To analyze the impedance response of symmetrical cells, pre-suspensions containing 35.13 wt% of 10XDC, 32.42 wt% of NiO, 29.55 wt% of terpineol, 2.90 wt% BYK P-104 were prepared. To form a slurry, 16 wt% of a transport agent (15 wt% ethyl cellulose [10cps]

dissolved in 85 wt% terpineol) was added to the pre-suspension. The layers were symmetrically printed on ~200 µm-thick 8YSZ electrolyte substrates with the same equipment and methods described for layered systems before. The layers were sintered at 1400 °C for 5 h. A NiO layer was applied on top to improve the contact between the Ni-10XDC layers and the Pt-mesh electrodes. The cells were reduced in-situ at 900 °C for 3 h in Ar/ 3 % H_2.
Impedance measurements were conducted in Ar/ 3 % H_2 at temperatures between 200–400 °C and 600–900 °C using frequencies between 10^6–10^{-1} Hz with a Novocontrol Alpha-A frequency analyser in a tube furnace.
The recorded spectra have been checked for linearity and time-invariance by the Linear-Kramers-Kronig Transformation using the software “Lin-KK” [28]. The calculated residuals indicate valid spectra.
An equivalent circuit model was used to fit the spectra. Subsequently, the polarization resistance (R_{pol}) at higher temperatures (600–900 °C) and the characteristic frequencies (*f_max*) of the respective elements containing a resistor in parallel with a constant phase element (R-CPE) and the ohmic resistance (R_{ohm}) of the electrolyte at lower temperatures (200–400 °C) were calculated. Further information about the fitting and evaluation of the impedance spectra are given in the SI.
To investigate the influence of porosity at the 8YSZ interface, symmetrical Ni-10GDC cells were prepared and compared to symmetrical cells which contained a 10GDC barrier layer between the Ni-10GDC electrode and the 8YSZ electrolyte. The layers were printed on ~200 µm thick 8YSZ substrates. The 10GDC barrier layer has a thickness of ~5–7 µm and the Ni-10GDC electrodes of ~7–10 µm. One set of cells with barrier layers were co-sintered with the electrode at 1400 °C for 3 h. In another set of cells, the barriers were sintered at 1300 °C for 3 h before electrode printing, and the electrodes were subsequently sintered at 1400 °C for 3 h. The electrodes contain 45 wt% NiO and 55 wt% 10GDC. The cells were measured with impedance spectroscopy as described in the paragraph above. An illustration of the used symmetrical cells is shown in Figure 1.

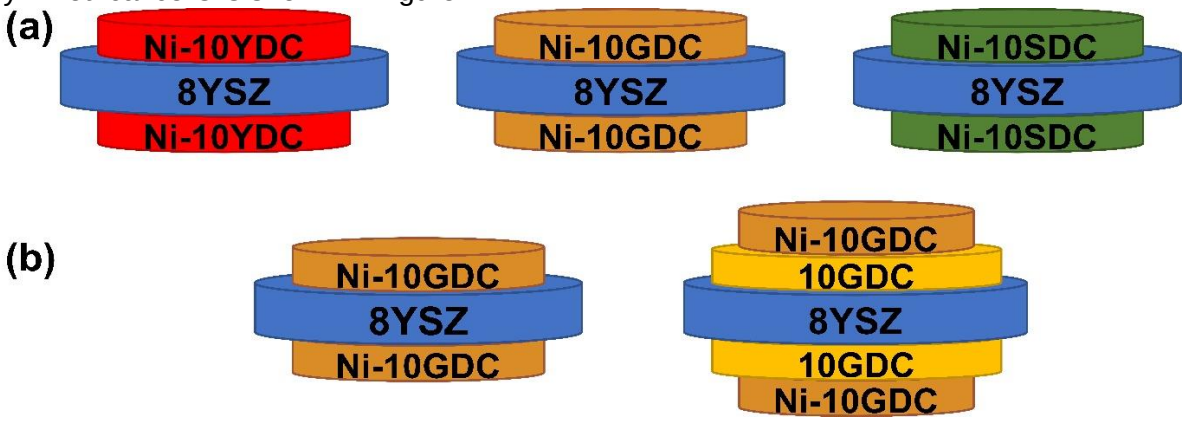

Figure 1: Illustration of the symmetrical Ni-10XDC cells used for impedance spectroscopy and SEM-analysis to investigate (a) the dopant influence and (b) the influence of porosity at the interface with 8YSZ.

Scanning electron micrographs of polished cross-sections of all symmetrical cells were recorded with a Zeiss EVO equipped with a back scattered electron detector to determine interdiffusion lengths.

2.4 Determination of ionic conductivity, grain size and porosity

The ionic conductivity of 8YSZ/10XDC pellets sintered at 1400 °C for 5 h were measured between 500–900 °C in air, again using impedance spectroscopy with a similar setup described above for symmetrical cells. The grain and grain boundary impedance were added up to the total ionic impedance of the ceramic using the brick-layer model [29, 30].

Furthermore, the average grain size of those pellets was calculated from SEM images obtained on polished, thermally etched cross-sections, using the software Fiji [31].
The number of grains (at least 100) which are intersected by straight lines were counted and divided by the length of the lines. Six pictures of different magnifications were investigated, and the calculated grain size was averaged. Beforehand, the pellets were thermally etched at 1300 °C for 0.5 h to increase the visibility of the grain boundaries.
Porosity was estimated using the Archimedes` method in water to obtain the relative density.

3 Results

3.1 Powder properties

The particle size distribution and specific surface areas of the used powders are given in Table 1.

Table 1: Particle size distributions and specific surface areas of the used powders.

Material	d10 (µm)	d50 (µm)	d90 (µm)	SSA (m^2/g)
10YDC	0.07	0.11	1.10	16.2
10GDC	0.07	0.11	0.23	12.1
10SDC	0.07	0.10	0.19	10.5
8YSZ	0.16	0.54	1.51	13.2
NiO	0.40	0.66	1.19	4.8

The 10XDC powders show comparable particle size distributions, except for the d_{90} of 10YDC which is approximately 5 times higher than the d_{90} of 10GDC and 10SDC. Taking into account the higher specific surface area of 10YDC, it is likely that the ultrasonic treatment before the particle size analysis was not able to break all agglomerates. Due to the ball milling process before using these powders to fabricate pellets or slurries, it can be assumed that agglomerates have been broken up.
Figure 2 shows in-lens electron microscope pictures of the used 10XDC powders. The micrographs reveal similar particle shape and the tendency of the powders to agglomerate. Overall, the powders are similar enough that individual processing steps do not have to be adapted for each one.

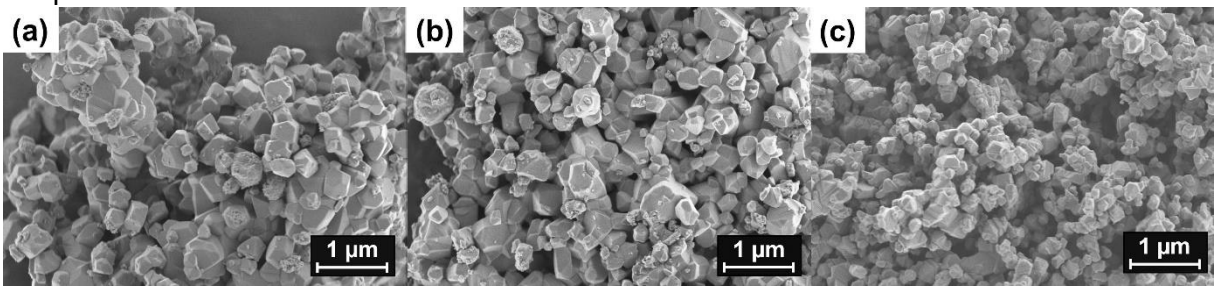

Figure 2: Morphology of the starting powders: (a) 10YDC, (b) 10GDC and (c) 10SDC.

3.2 Microstructure of sintered pellets

In general, the microstructure of the sintered 8YSZ/10XDC pellets (shown in Figure 3) is comparable.

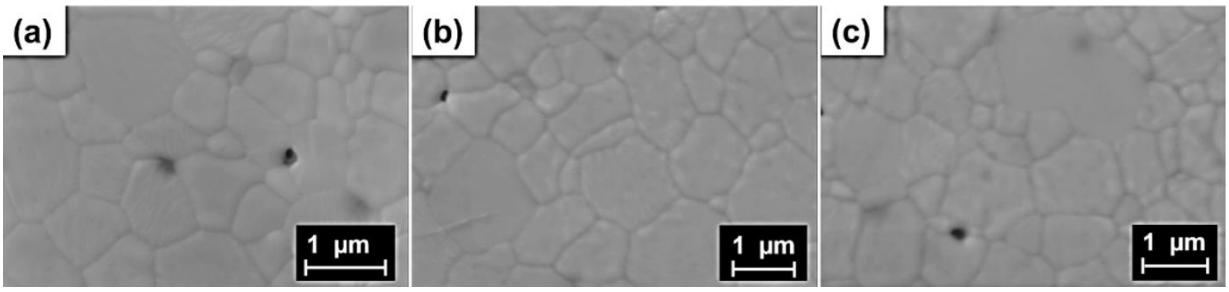

Figure 3: Microstructure of (a) 8YSZ/10YDC, (b) 8YSZ/10GDC and (c) 8YSZ/10SDC pellets sintered at 1400 °C for 5 h and subsequently thermally etched at 1300 °C for 0.5 h.

8YSZ/10GDC shows a slightly larger average grain size compared to 8YSZ/10YDC and 8YSZ/10SDC (see Table 2) pellets indicating slightly higher cation mobility. The grain size for Y or Sm as a dopant in ceria in the mixture with 8YSZ does not differ. The density of the 8YSZ/10XDC pellets is comparable, yielding approximately above 96% of the theoretical density (see Table 2).

Table 2: Average grain size and relative density of the sintered 8YSZ/10XDC pellets.

Material	Average grain size (µm)	Relative density (%)
8YSZ/10YDC	0.65 ± 0.09	97 ± 2
8YSZ/10GDC	0.88 ± 0.12	96 ± 2
8YSZ/10SDC	0.65 ± 0.08	98 ± 1

3.3 Interdiffusion in powder mixtures

The complete miscibility of zirconia and ceria and the interdiffusion during high temperature treatment is well documented [14-16, 32-34]. Since interdiffusion kinetics depend on the contact area between particles, powders with similar particle size distributions and shapes have been chosen for the different dopants in 10XDC. Although, a certain similarity of the used powders is given, the obtained results are dependent on the properties of the used powders and its influence cannot fully be separated from the influence of the dopant.
The other parameters that influence interdiffusion are temperature and time. Therefore, the phase formation and content inside the mixed 8YSZ/10XDC pellets were analyzed as a function of temperature while the sintering time has been held constant (5 h).
Figure 4 (a–c) shows the diffraction patterns of 8YSZ/10XDC pellets after sintering at different temperatures. The Bragg reflections of the (111) crystallographic plane of 8YSZ and 10XDC is indicated with a black line and a black dashed line respectively. No additional phases are visible apart from 8YSZ, 10XDC and their intermixing phases.
No intermixing is apparent after sintering at 1000 °C.
With rising sintering temperature, the diffraction patterns show a shift in the position of the (111) diffraction line to higher 2θ angles for 8YSZ and to lower 2θ angles for 10XDC respectively, indicating intermixing.
The 8YSZ lattice expands due to an increasing amount of Ce and the respective dopant X dissolving into it, leading to a shift of the reflections to lower 2θ angles according to Bragg`s law (sin(Θ) ~ 1/a). On the other hand, the XDC lattice contracts with increasing Zr and Y content shifting the reflections to higher 2θ angles. These phases are denoted as YSZ_{XDC} and XDC_{YSZ} respectively.
After sintering at 1300 °C, only one single fluorite phase is visible for all dopants. They differ in the full width at half maximum (FWHM) of the reflections for the different dopants, indicating differences in lattice disorder and different amounts of fully intermixed phases. The FWHM is highest for Sm, followed by Y and lowest for Gd, indicating a higher amount of lattice order and intermixing for 10GDC followed by 10YDC and 10SDC.

For all dopants, the FWHM decreases again when increasing the sintering temperature to 1400 °C, indicating larger crystallites and less strain in the lattice.
To analyze the relative phase content and its development, a Rietveld analysis was performed (the error is estimated to be about ~ 1%). Since the solid solutions follow Vegard´s law, meaning a linear relationship between lattice parameter and stoichiometry (see Figure S1, SI), it is possible to determine the lattice parameter of each phase, calculate the stoichiometry of the phases and then determine the relative phase content. Note that for the purpose of this analysis, the stoichiometry of the parent compounds and the fully intermixed phase are fixed, whereas the intermediate phases YSZ_{XDC} and XDC_{YSZ} have a varying stoichiometry over the temperature range. This is necessary since the interdiffusion is a continuous process, meaning that the only defined stoichiometries are the starting compounds and the fully intermixed result. Figure 5 (a–c) shows the results of the Rietveld refinement for 8YSZ/10XDC powder mixtures. Discrete data points are shown, the lines are a guide to the eye.
In general, the amounts of the pure 10XDC-phases decrease faster than the pure 8YSZ phase independent of the dopant in ceria. The YSZ-rich mixed phases (YSZ_{XDC}) increase faster in amount than the 10XDC rich mixed phases (XDC_{YSZ}) indicating a higher interdiffusion coefficient for Ce and the respective dopant X compared to Zr and Y.
Considering the dopant in ceria and its influence on the interdiffusion behavior with 8YSZ, changes in the relative phase distribution are observable. The YSZ_{GDC} and GDC_{YSZ} phases form at lower temperatures and in higher amounts compared to Y and Sm doped ceria. Also, the mixed phase forms at temperatures between 1200 and 1300 °C. For 8YSZ/10YDC mixtures, the mixed phase forms at higher temperatures between 1300 and 1400 °C. For 8YSZ/10SDC mixtures, no completely mixed phase is formed up to 1400 °C and the amount of YSZ_{SDC} and SDC_{YSZ} is lower at all given temperatures compared to YSZ_{GDC}, GDC_{YSZ} and YSZ_{YDC} and YDC_{YSZ}. Also, for 8YSZ/10SDC two YSZ rich mixed phase were observed ($YSZ1\_{SDC}$ and $YSZ2\_{SDC}$) and no formation of a fully intermixed phase.
This may indicate an influence of the dopant or dopant radius on the interdiffusion kinetics and the formation of mixing phases in powder mixtures with 8YSZ.
The intermediate phases are kinetically stabilized phases, since the system has not had sufficient time to fully intermix. In this investigation, we intentionally limited the sintering time to 5 hours in order to determine the degree of intermixing that can be expected during sintering of the fuel electrode supported half-cell.

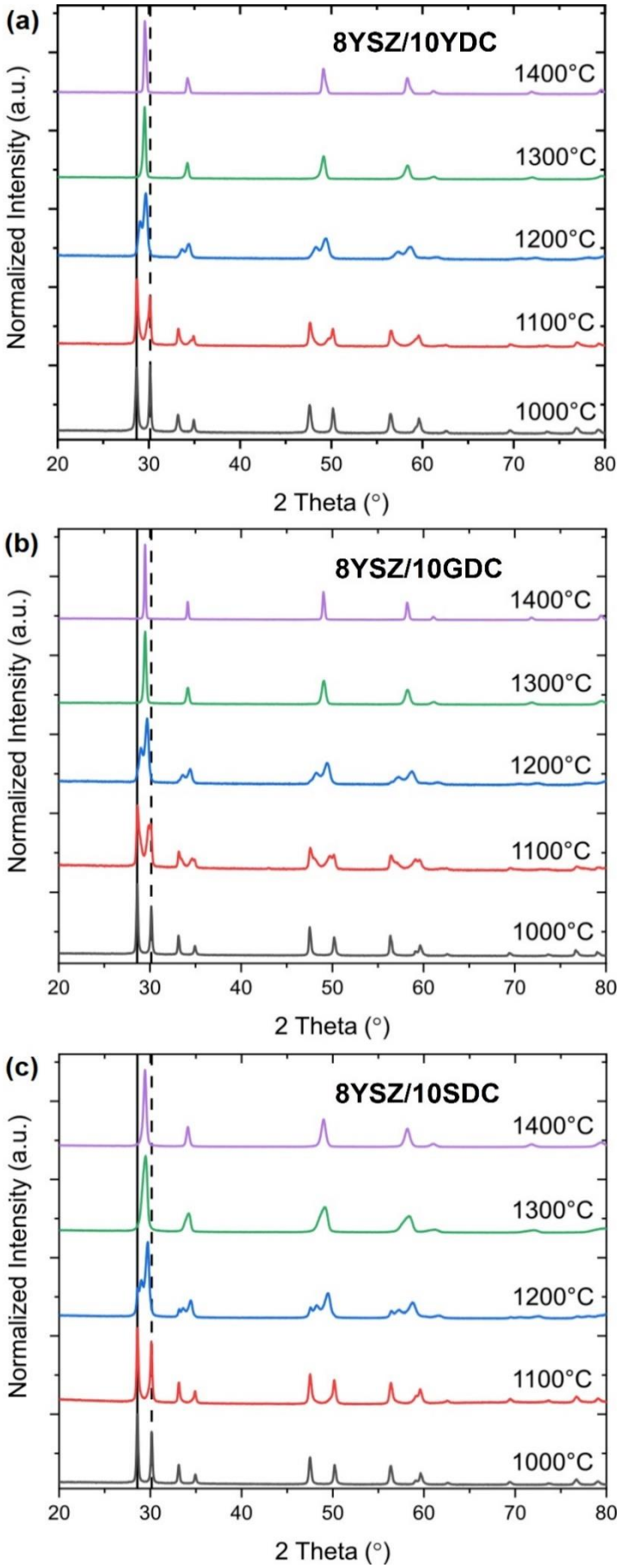

Figure 4: Diffractograms of 8YSZ/10YDC, 8YSZ/10GDC and 8YSZ/10SDC powder mixtures sintered at temperatures between 1000–1400 °C for 5 h.

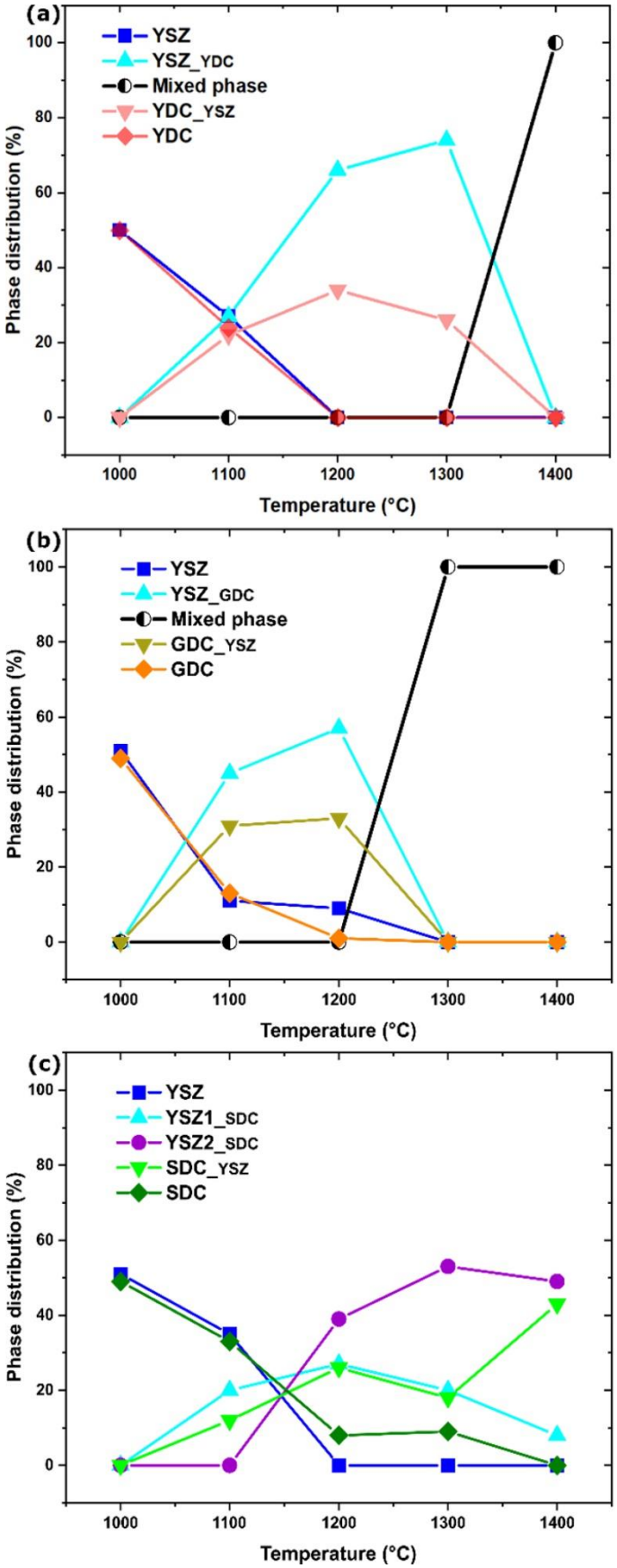

Figure 5: Relative phase distribution of (a) 8YSZ/10YDC, (b) 8YSZ/10GDC and (c) 8YSZ/10SDC pellets sintered in air at temperatures between 1000–1400 °C for 5 h. Lines are a guide to the eye.

3.4 Ionic conductivity of sintered pellets

The total ionic conductivity of 8YSZ/10XDC pellets is shown in Figure 6. The nominal stoichiometry of the YDC/YSZ and GDC/YSZ samples according to Rietveld refinement is: $Y_{0.127}Zr_{0.487}Ce_{0.387}O_{2-\delta}$ and $Y_{0.084}Zr_{0.487}Gd_{0.043}Ce_{0.387}O_{2-\delta}$, respectively. The 8YSZ/10SDC sample contains three phases: $Y_{0.105}Zr_{0.605}Sm_{0.029}Ce_{0.261}O_{2-\delta}$, $Y_{0.090}Zr_{0.520}Sm_{0.039}Ce_{0.351}O_{2-\delta}$ and $Y_{0.078}Zr_{0.452}Sm_{0.047}Ce_{0.423}O_{2-\delta}$. The ionic conductivities are compared to dense 8YSZ and 10GDC ceramics. The 8YSZ/10XDC pellets possess ionic conductivities which are about one order of magnitude lower compared to 8YSZ. The values are in agreement with the conductivity values determined in literature for 8YSZ/10GDC and their solid solutions and it is reported that YSZ and GDC/SDC mixtures possess the lowest ionic conductivity when they form a mixed phase with a stoichiometry of $8YSZ_{0.5}$- $YDC_{0.5}$/$GDC_{0.5}$/$SDC_{0.5}$ [14, 34-36]. It was shown that this is due to the lower mobility of the charge carriers compared to the pure material, which is likely a result of the increasing lattice disorder in the intermixed phases [22].
Nevertheless, there is no significant difference in the ionic conductivities for the different dopants in ceria within the accuracy of the measurement and the applied fit. Comparing 8YSZ/10YDC and 8YSZ/10GDC regarding the calculated phase distribution, no difference in ionic conductivity is expectable, except the influence of the dopant on conductivity. Although, 8YSZ/10SDC do not form a fully intermixed phase, no change in ionic conductivity is observable. Hence, the lower degree of mixed phase formation shows no impact on ionic conductivity in bulk material. Furthermore, the dopant does not alter the ionic conductivity in densely sintered mixed 8YSZ/10XDC pellets, although 10SDC exhibits slightly higher ionic conductivity compared to 10GDC [37, 38].

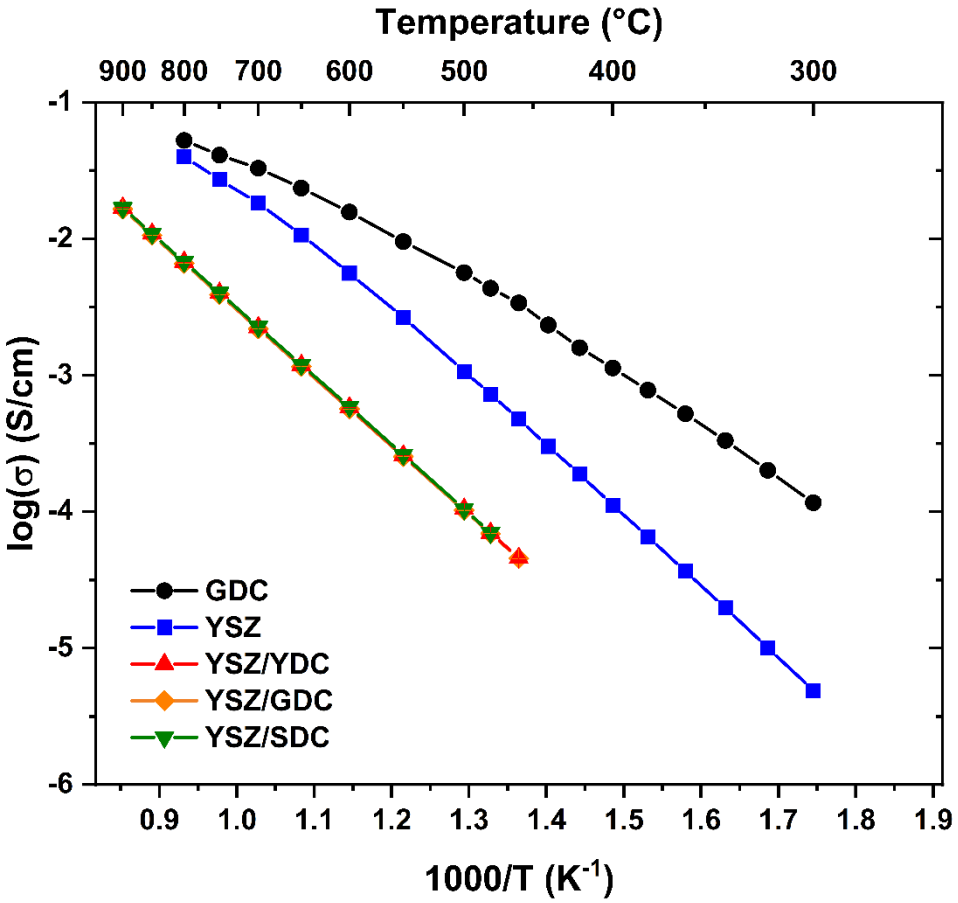

Figure 6: Ionic conductivity of dense 10GDC, 8YSZ, 8YSZ/10YDC, 8YSZ/10GDC and 8YSZ/10SDC pellets sintered at 1400°C for 5 h measured at temperatures between 500–900 °C in Ar/ 3%H_2. Lines are a guide to the eye.

3.5 Interdiffusion in layered screen-printed systems

To analyze the degree of interdiffusion in layered systems, backscattered electron imaging is used instead of EDS mapping. The backscattered electrons enable a better spatial resolution due to the much smaller scattering volume compared to the excitation volume of EDS (which is ~1 µm and is in the range of the measured interdiffusion lengths). The backscattered electron coefficient η is depended on the atomic number Z resulting in different intensities and contrasts in the recorded backscattered electron image (Z-contrast). Since in polyphase specimens Z varies, the backscattered electron image contains different contrasts. The higher Z the brighter the phase appears. Therefore, the material contrast is suitable to resolve the original yttria- stabilized zirconia and doped ceria phases as well as their intermixing phases, since they significantly vary in Z [39]. Furthermore, the process of using material contrast is common practice in the solid oxide cell (SOC) community and was evaluated for the air side of a SOC by Wankmüller *et al.* [40]. To resolve the interdiffusion length of Ce and X into the dense 8YSZ substrate, the variation in material contrast was investigated across the interdiffusion zone.

An exemplary SEM picture of the analyzed cross-sections for every dopant is shown in Figure 7 (a–c). Since the interface shifts during sintering due to the difference in diffusion coefficients, the position of the interface has been estimated using material contrast. The printed layers are porous but the interface is homogenously covered with XDC. The interdiffusion zone shows no clear horizontal boarder but a wavelike form. This might be due to statistical effects or a gradient in chemical potential.

The interdiffusion lengths have been estimated up to the furthest point of the contrasted zone. The average grey value of the boundaries of the XDC and YSZ layers were measured using the software Fiji by utilizing data points which are located outside of the interdiffusion zone. The length of the interdiffusion zone was then measured by drawing a straight line between the boundaries of the 10XDC and 8YSZ grey value. Error bars show the standard deviation of at least seven evaluated pictures.

The estimated diffusion lengths are plotted in Figure 8. A slight change in the diffusion length is observable for Gd compared to Y and Sm as dopant in the 8YSZ/10XDC diffusion couples. The results are consistent with the obtained phase distribution in powder mixtures, where 10GDC shows the highest amount of interdiffusion. This also indicates a slight influence of the dopant size on the diffusion coefficient of the respective cations. The results are similar compared to the measured diffusion lengths by Ozawa *et al.* for YSZ and CeO_2 diffusion couples [41]. The difference in material contrast indicates the formation of a mixed phase which is known to be less conductive than 8YSZ and 10XDC and may limit the performance of an FESC.

3.6 Interdiffusion in the presence of NiO

NiO is typically part of fuel electrodes to guarantee sufficient electrical conductivity and catalytic properties. We observed an enhancement of the cation diffusion in fluorite structures in the presence of NiO. Additionally, porosity was formed at the interface of symmetrical Ni-10XDC cells with an 8YSZ electrolyte. Cross-sections of the cells after impedance measurements are shown in Figure 9 (a–c). The diffusion lengths into 8YSZ increased for all samples, independent of the dopant (see Figure 9 (d)).

In addition, EDS line scans and maps were performed to confirm the results and to measure the interdiffusion of Ni in symmetrical cells since its material contrast is similar to 8YSZ. The diffusion lengths of Ni are similar or slightly shorter compared to Ce and X meanwhile enhancing their interdiffusion kinetics. This information is not shown here but in Figure S2–7, SI.

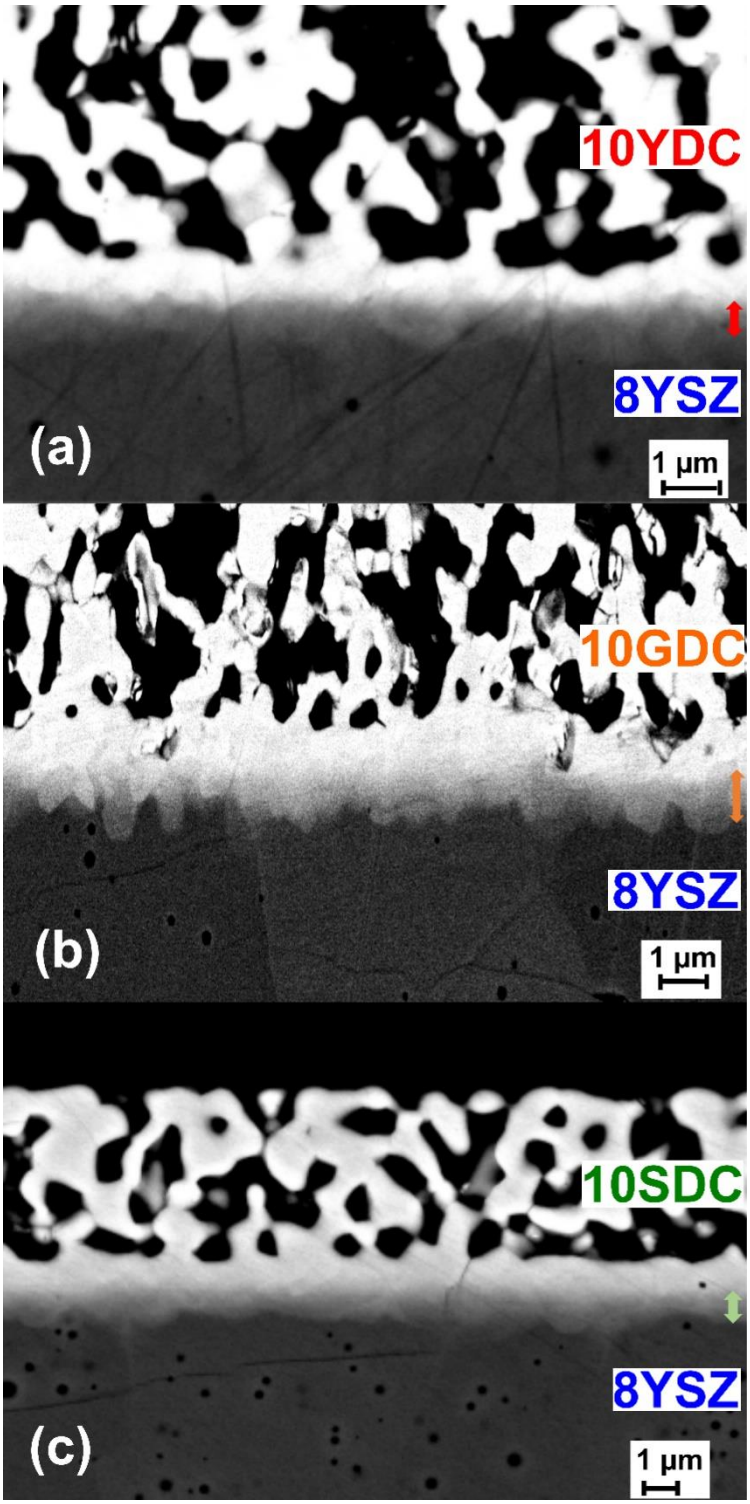

Figure 7: Backscattered electron images of cross-sections of screen-printed doped ceria layers (porous light layer on top) on dense 8YSZ substrate (bottom dark layer) for (a) 10YDC, (b) 10GDC and (c) 10SDC sintered at 1400 °C for 5 h.

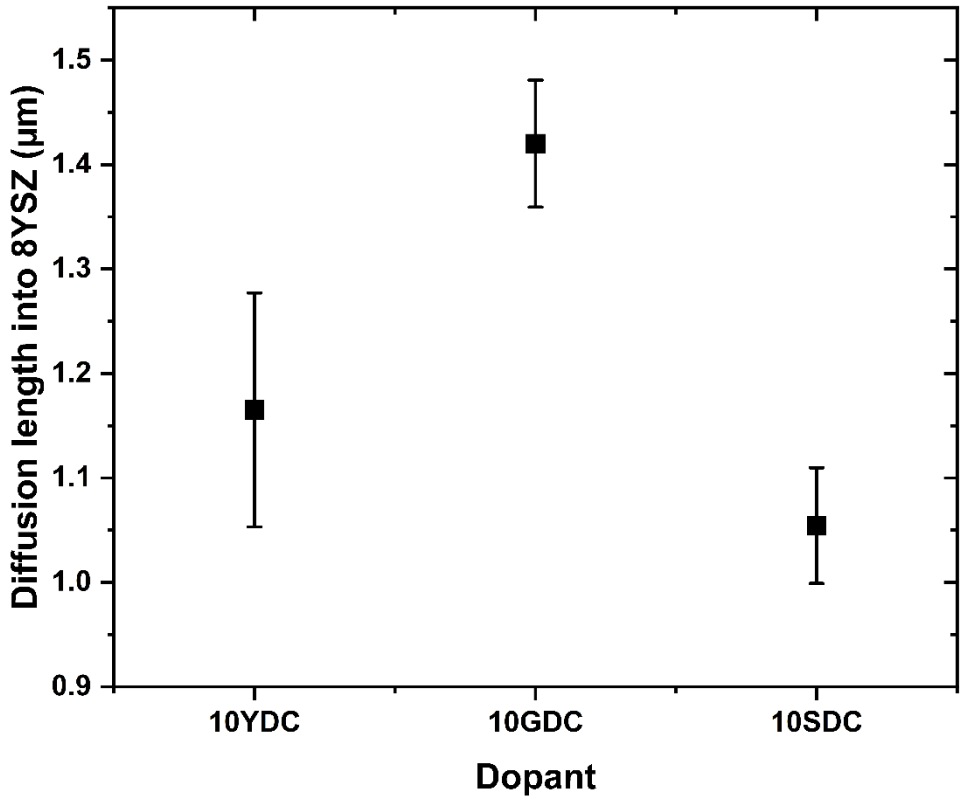

Figure 8: Diffusion lengths of the cations Ce and X of screen-printed 10XDC layers into dense 8YSZ sintered at 1400 °C for 5 h.

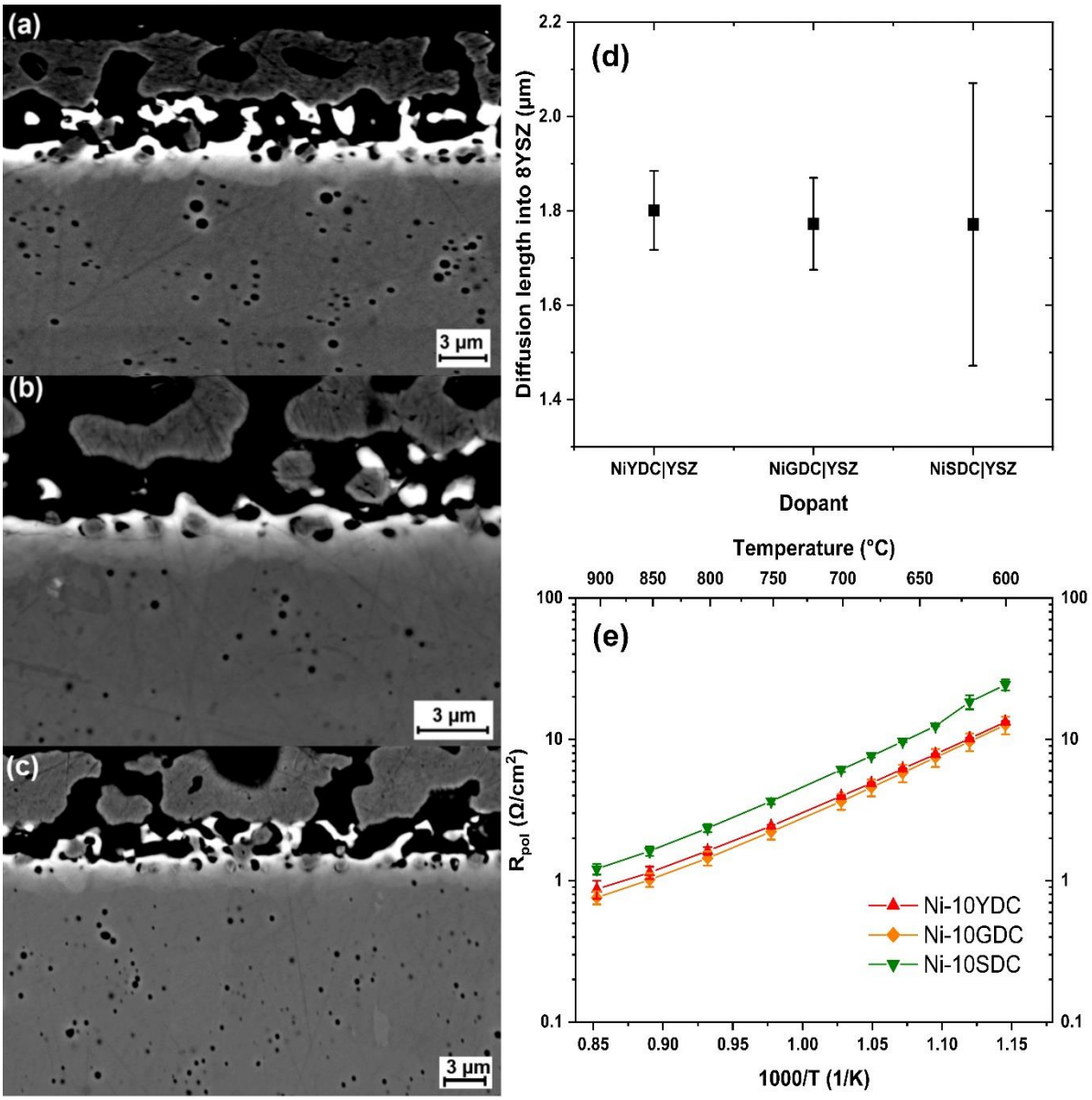

Figure 9: Backscattered electron images of cross-sections of symmetrical (a) Ni/Ni-10YDC/8YSZ cells, (b) Ni/Ni-10GDC/8YSZ and (c) Ni/Ni-10SDC/8YSZ cells sintered at 1400 °C for 5 h. (These cells were used for impedance measurements in section 3.6.1). (d) Diffusion lengths of Ce and X into 8YSZ of Ni-10XDC symmetrical cells. (e) Polarization resistance of Ni-10XDC symmetrical cells measured at temperatures between 600–900 °C in Ar/ 3%H_2; lines are a guide to the eye.

3.7 Impedance response of symmetrical cells

3.7.1 Impedance response of differently doped symmetrical cells

Symmetrical cells with Ni-10XDC layers were investigated with impedance spectroscopy. The characteristic frequency f_max for grains and grain boundaries were compared to dense bulk 8YSZ and 10GDC ceramics. Since f_max does not show a significant difference between cells with different dopants, the results are not shown here but in the SI, Figure S9. The ohmic resistance of the Ni-10XDC cells also shows no significant difference (see Figure S10, SI).
The polarization resistances of the Ni-10XDC cells are shown in Figure 9 (e). Error bars show the standard deviation of three samples. The results show no significant difference between Gd- and Y- doped electrodes, and a higher polarization resistance for Sm-doped electrodes. On the one hand, this result is counterintuitive since Sm-doped ceria possesses the highest ionic conductivity. On the other hand, ceria with Sm as a dopant exhibits lower reducibility [42].

Although all cells have been prepared in the same way, microstructural features could influence the performance of the electrode since the starting powders are not fully alike. Especially the specific surface area of 10SDC is lower compared to 10GDC and 10YDC. Therefore, the higher polarization resistance of Ni-10SDC is likely a result of microstructural differences.
These results indicate that the differences in interdiffusion between the three ceria phases have a negligible influence on the polarization resistance.

3.7.2 Influence of porosity on the impedance response of symmetrical cells

The impedance response of symmetrical cells with Ni-10GDC electrodes with and without 10GDC barrier layer were measured.
Cross-sections of the symmetrical cells are shown in Figure 10 (a–c). It is clearly visible again that incorporation of NiO into a doped ceria layer which is in direct contact with the 8YSZ interface leads to emerging porosity in the most electrochemically active area, while a doped ceria barrier layer prevents the forming of porosity at the 8YSZ interface during sintering. The diffusion lengths of Ce and Gd into the 8YSZ electrolyte are shown in Figure 10 (d). Diffusion lengths of Ce and X are slightly longer if NiO is present in the layer adjacent to the 8YSZ electrolyte. If the barrier is co-sintered with the electrode, diffusion lengths are about 1 µm shorter compared to sequentially sintered barrier and electrode layer. The polarization resistances of cells without barrier layer, co-sintered electrode/barrier layers and sequentially sintered electrode and barrier layers are shown in Figure 10 (e). Error bars show the standard deviation of three samples. Symmetrical cells without a barrier layer show significantly higher polarization resistances compared to cells with a barrier layer. Interestingly, whether the electrode and barrier layers were co-sintered or sequentially sintered does not influence the polarization resistance, although two sintering steps increase the length of interdiffusion of Ce and Gd into 8YSZ significantly.
In Figure 11 the ohmic resistance of the 8YSZ electrolyte and (if present) additionally the 10GDC barrier is shown. The ohmic resistance for cells with barrier layer is slightly but significantly higher compared to cells without barrier. Cells with co-sintered and sequentially sintered layers do not vary in ohmic resistance at temperatures between 340–280 °C. At lower temperatures the cells with co-sintered layers show slightly higher ohmic resistance. The co-sintered cells show significantly shorter interdiffusion lengths, leading to the conclusion that the influence of a mixed phase with reduced conductivity on the total ionic conductivity is negligible in these systems, while the polarization resistance is dependent on the microstructure at the interface.

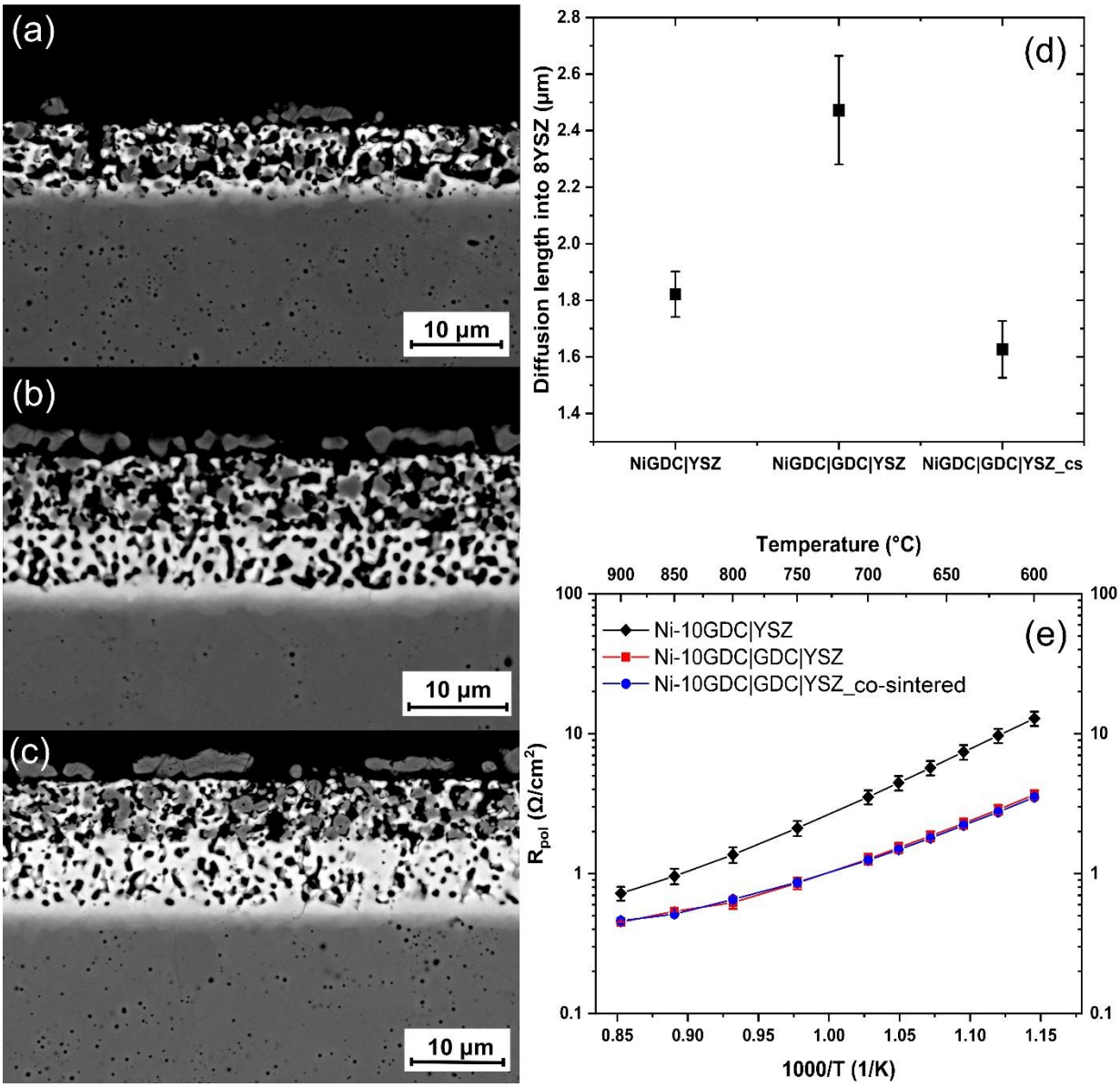

Figure 10: Backscattered electron images of cross-sections of symmetrical Ni-10GDC cells (a) without a 10GDC barrier layer, (b) with a sequentially sintered 10GDC barrier layer and (c) with a co-sintered 10GDC barrier layer. (d) Diffusion lengths of Ce and Gd into 8YSZ of Ni-10GDC symmetrical cells with (sequentially and co-sintered) and without barrier layer. (e) Polarization resistance of Ni-10GDC symmetrical cells with (sequentially and co-sintered) and without barrier layer measured at temperatures between 600–900 °C in Ar/ 3%H_2; lines are a guide to the eye.

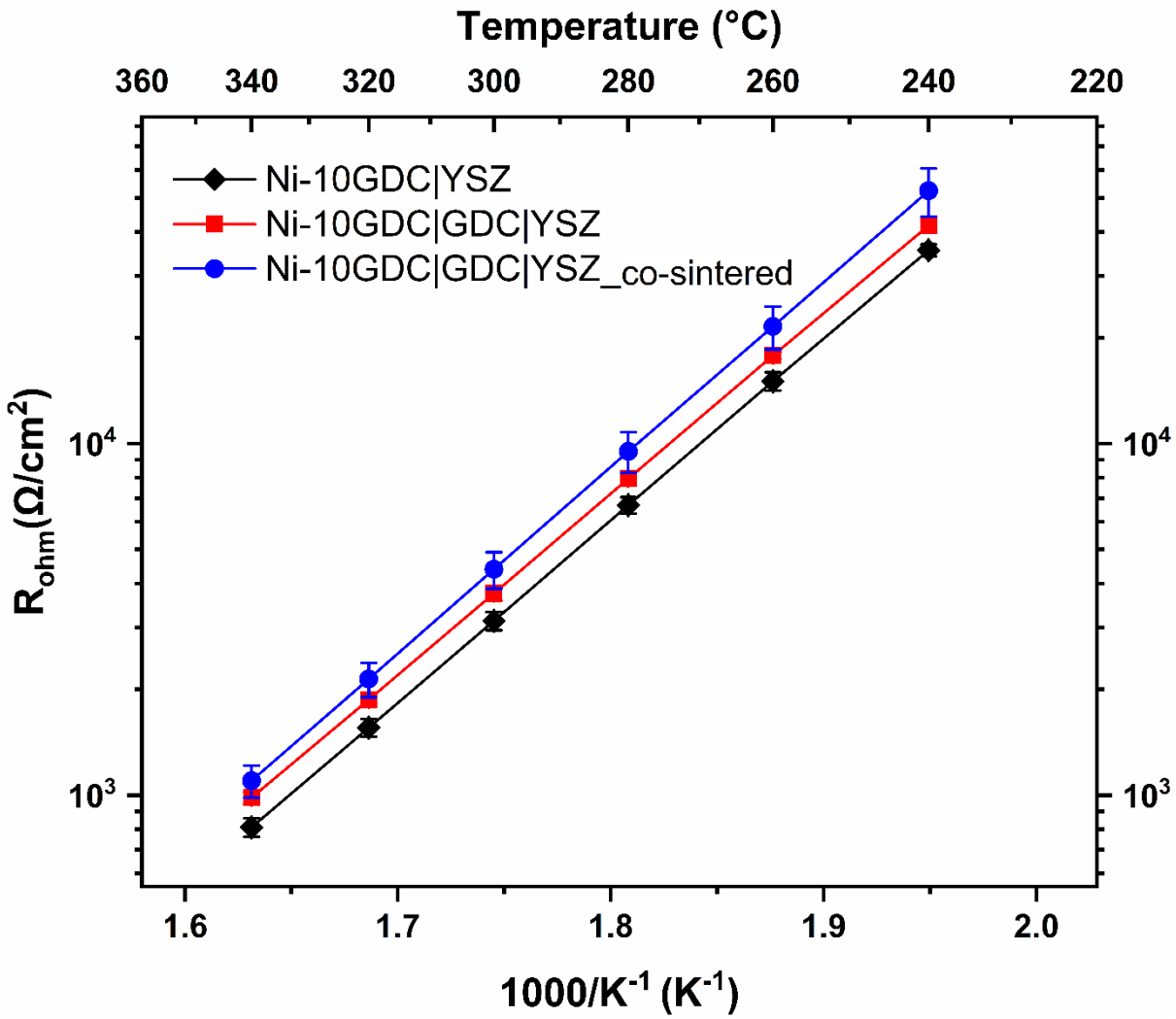

Figure 11: Ohmic resistance of symmetrical Ni-10GDC cells and cells with 10GDC barrier layer (sequentially or co-sintered with the electrode) measured at temperatures between 240–340 °C in Ar/ 3%H_2. Lines are a guide to the eye.

4 Discussion

4.1 Consequences of interdiffusion

The suppression of interdiffusion between two functional layers is generally desirable. But if high temperature manufacturing steps are involved, interdiffusion seems to be inevitable. There are two consequences of interdiffusion in the manufacturing process of a common FESC with a Ni-10XDC fuel electrode and an 8YSZ electrolyte layer: The formation of a mixed phase with reduced conductivity, and microstructural changes in terms of porosity at the electrode/electrolyte interface.

Regarding the formation of the mixed phase, shorter diffusion lengths should be beneficial since less amount of mixed phase is formed.

A fully intermixed 8YSZ/10XDC phase exhibits the lowest ionic conductivity, but in practice a gradient in stoichiometry is present which leads to a gradient in ionic conductivity in the interdiffusion zone (also confirmed by EDS line scans in Figure S2-4, SI). Symmetrical cells with sequentially sintered barrier and electrode show significantly longer interdiffusion lengths of Ce and Gd into the 8YSZ electrolyte compared to co-sintered cells but no difference in ionic conductivity. Whereas increasing the electrolyte thickness by adding a porous barrier increases ionic conductivity measurably. Therefore, if the electrolyte has a certain thickness

(here ~200 µm) a narrow and graded interdiffusion zone shows no significant influence on ionic conductivity of the electrolyte. In FESC a thinner electrolyte of about 10 µm is present. In this case the ratio of electrolyte thickness to the length of the interdiffusion zone changes from about 133 to 7, which might lead to a measurable influence on ionic conductivity and cell performance.
Porosity at the electrode/electrolyte interface as a consequence of interdiffusion shows a severe influence on the polarization resistance, where cells with porous interfaces have drastically higher values. The reason could be an inferior contact between the fuel electrode and electrolyte layer. Porosity at the interface might also lead to less electrochemically active area at the interface. In general, if there is no contact between the fuel electrode and the electrolyte, the flow of O^{2-} from the electrolyte to the fuel electrode is prevented. This would also be the case in an actual FESC. Therefore, also in case of a thinner electrolyte, prevention of porosity at the electrode/electrolyte interface has a more beneficial impact on cell performance than prevention of a mixed phase with lower conductivity.
Nenning *et al.* showed that a more homogeneous and adhesive contact at the direct electrolyte interface improves polarization resistance. The improved contact was realized by adding a 10GDC layer between the 8YSZ electrolyte and Ni-10GDC electrode. The cells without barrier are just connected to the electrolyte by some sintering necks. Although no porosity was found (likely due to the lower sintering temperature of 1100 °C) this study also indicates that less contact area at the direct electrolyte interface increases polarization resistance of the electrode, similar to this study [43].
Although the dopant modifies the interdiffusion kinetics slightly, it cannot prevent formation of porosity at the interface while porosity is not formed in the absence of NiO.
It is interesting to compare our findings regarding the effectiveness of a 10GDC barrier layer between YSZ and NiO/GDC to the barrier layers commonly applied on the air side of a cell.
It has been shown that an interdiffusion zone between 10GDC and 8YSZ is the key to prevent the formation of insulating $SrZrO_3$, whereas the decrease in ionic conductivity in the interdiffusion layer has a negligible impact on cell performance. Contrary to our findings on the fuel side, co-sintering of the GDC barrier with a LSCF electrode on the air side has tremendously negative effects on cell performance. The difference is likely the transport mechanism of Sr during electrode sintering, where there are strong indications for gas-phase transport of the Sr species to the electrolyte interface. Therefore, the barrier on the airside has to be sintered sequentially, and at higher temperatures of at least 1300 °C to form a sufficiently dense interdiffusion layer [44].
Since the interdiffusion processes on the fuel side is driven mainly by bulk and surface diffusion, co-sintering does not affect performance since the NiO is much slower to arrive at the interface compared to gaseous Sr-(hydr)oxides.
Hence, the prevention of porosity at the electrolyte interface on the fuel side has the most beneficial impact on polarization resistance and overall cell performance, and the additional 10GDC barrier layer is crucial if porosity cannot be prevented otherwise.

4.2 Possible reasons for porosity formation

The formation of porosity at an interface due to diffusion is known as Kirkendall porosity. If the cations of the adjacent layers possess sufficiently different diffusion coefficients, more cations diffuse from one layer into the other than vice versa. This leads to material depletion in the layer where the cations possess the higher interdiffusion coefficient, and thus to the formation of Kirkendall voids in the vicinity of the interface. Normally, the formation of Kirkendall voids can be expected on the XDC side at the interface since more Ce and X atoms diffuse into 8YSZ compared to Zr and Y atom diffusion into XDC in a given time frame [23, 25, 45]. Interestingly, Kirkendall voids were not observed in the layered structures when NiO was

absent. The addition of NiO to the electrode cermet seems to enhance the interdiffusion coefficient of Ce and X into 8YSZ. This leads to an increase in the difference of the interdiffusion coefficients of Zr and Y compared to Ce and X which is then sufficiently high to generate porosity.
In former experiments, Lenser *et al.* [22] observed the enhancement of interdiffusion in the presence of NiO between 8YSZ and 10GDC in powder mixtures whereas Tsoga *et al.* [25] report a suppression of Ce into a YSZ lattice.
Smaller amounts of NiO, below the solubility limit, are observed to enhance the sinterability of 8YSZ and 10GDC. Presumably, doping the host lattice with Ni increases volume diffusion. Below the solubility limit, the grain boundary diffusion seems not to be influenced (just if some decomposition reaction of NiO precursors take place in the initial state of sintering). Above the solubility limit, NiO tends to segregate at grain boundaries and decreases the sinterability due to pinning effects [46, 47].
It should be added that it is also proposed that sinterability might be increased due to promoted grain boundary mobility as a result of the distortion of the surrounding lattice by Ni [48]. Ni diffuses during sintering of Ni-GDC|GDC layered system and causes microstructural modifications which is believed to be due to the formation of Ni interstitials and oxygen vacancies resulting in defect clusters and inhomogeneous microstructures due to altered ion diffusion [49].
Furthermore, the influence of NiO as sintering aid in the fabrication of proton conducting $Ba(Zr,Ce,Y)O_{3-\delta}$ has been reported. Although not possessing the fluorite crystal structure but the perovskite structure, some of the proposed mechanisms should be mentioned here, since some of the NiO induced modifications might be similar. By doping the host lattice with Ni, cation defects, oxygen vacancies as well as electronic defects are created which accelerate phase transitions and sintering. The prevention of the $BaZrO_{3-\delta}$ seems to be of importance. It was shown that using sintering aids with similar ionic radius to Zr^{4+} and a valence of +II promote sintering the most [50]. However, if the NiO fraction is too large it tends to aggregate [51]. Another possible mechanism is the formation of a transient liquid phase respectively occurrence of liquid flow which accelerates cation diffusion and thus sintering [52].
Based on the suggested mechanisms in literature and the findings in this study, a plausible hypothesis would be the doping of the 10GDC grains by adjacent NiO grains during sintering. The doping with Ni would lead to cationic defects (Ni might be located on a regular lattice site or an interstitial site) and to the formation of oxygen vacancies which would affect volume diffusion. This would be coherent with the data presented in the former sections, where it was shown that the dopant radius in ceria influences the interdiffusion with 8YSZ, whereas Ni even possess a lower average oxidation number of +II. This might lead to an even enhanced interdiffusion at the interface.
We clearly want to state, that the data raised in this study are not sufficient to elucidate the influence of Ni on interdiffusion and that the clarification of a mechanism is beyond the scope of this paper. But we think that it is of high importance to clarify the influence of NiO on the cation diffusion, especially in SOC materials, to understand occurring problems during fabrication and operation of SOC, and encourage the implementation of more appropriate experiments to understand the underlying mechanisms.

5 Conclusion

The influence of the dopant in ceria (Y, Gd, Sm) on the interdiffusion kinetics with 8YSZ was investigated in terms of powder mixtures, layered systems and symmetrical cells. The size of the dopant shows an influence on the interdiffusion behavior in terms of phase formation in thermodynamically driven systems. A slight change in the interdiffusion length at the interface of doped ceria layers and 8YSZ substrates was observed. The formation of Kirkendall voids

was not observed. Therefore, the size of the dopant in ceria appears to modify the overall interdiffusion kinetics with 8YSZ in the following order: Sm<Y<Gd.
No significant difference in ionic conductivity was measured for 8YSZ and differently doped ceria mixtures.
Furthermore, the influence of the dopant in symmetrical cells was investigated. Sm as a dopant in Ni-doped ceria electrodes shows a higher polarization resistance compared to Y and Gd, but microstructural influences cannot be excluded. The dopants and its interdiffusion behavior show no influence on the ohmic resistance of the electrolyte.
Sintering a cermet of NiO and doped ceria with an 8YSZ electrolyte leads to the formation of Kirkendall voids (porosity) at the electrochemical interface. Symmetrical cells with porosity at the interface show significantly higher polarization resistances compared to cells where the formation of porosity was prevented by adding a Gd-doped ceria barrier layer between electrode and electrolyte. Co-sintering of the barrier layer with the electrode compared to sequentially sintering of the layers shows no difference in polarization resistance. The added electrolyte thickness by a porous barrier layer adds more ohmic resistance to the electrolyte than a larger interdiffusion zone, indicating a negligible effect of the interdiffusion zone but a significant effect of the barrier layer on the ohmic resistance. However, the prevention of porosity at the interface in the investigated systems is more important for total cell impedance. It is not possible to prevent the formation of porosity at the electrochemical interface in the presence of NiO by modifying the dopant in ceria. Additionally, the choice of the dopant in the electrode does not alter the ohmic resistance after interdiffusion. Therefore, it is crucial to implement a doped ceria barrier layer between a cermet electrode consisting of NiO and doped ceria and an 8YSZ electrolyte to decrease polarization resistance significantly.

Acknowledgements

This work has been supported by the Deutsche Forschungsgemeinschaft (DFG) within the project SynSOFC II (275388933) which is gratefully acknowledged.
We gratefully thank Dr. Yoo Jung Sohn for performing Rietveld refinement and Dr. Martin Juckel for providing samples.

References

[1] D. Udomsilp, C. Lenser, O. Guillon, N.H. Menzler, Performance Benchmark of Planar Solid Oxide Cells Based on Material Development and Designs, Energy Technology 9(4) (2021) 2001062.
[2] C. Lenser, J. Zhang, N.H. Menzler, O. Guillon, Comparison of solid oxide fuel cell (SOFC) electrolyte materials for operation at 500 °C, Solid State Ionics 344 (2020).
[3] H. Jeong *et al.*, Utilization of Bio-Syngas in Solid Oxide Fuel Cell Stacks: Effect of Hydrocarbon Reforming, Journal of The Electrochemical Society 166 (2019) F137.
[4] N. Laosiripojana, S. Assabumrungrat, Catalytic steam reforming of methane, methanol, and ethanol over Ni/YSZ: The possible use of these fuels in internal reforming SOFC, Journal of Power Sources 163(2) (2007) 943-951.
[5] M.J. Escudero, I. Gómez de Parada, A. Fuerte, J.L. Serrano, Analysis of the electrochemical performance of MoNi–CeO_2 cermet as anode material for solid oxide fuel cell. Part I. H_2, CH_4 and H_2/CH_4 mixtures as fuels, Journal of Power Sources 253 (2014) 64-73.
[6] M.J. Escudero, C.A. Maffiotte, J.L. Serrano, Long-term operation of a solid oxide fuel cell with MoNi–CeO_2 as anode directly fed by biogas containing simultaneously sulphur and siloxane, Journal of Power Sources 481 (2021).
[7] M.S. Khan, S.-B. Lee, R.-H. Song, J.-W. Lee, T.-H. Lim, S.-J. Park, Fundamental mechanisms involved in the degradation of nickel–yttria stabilized zirconia (Ni–YSZ) anode

during solid oxide fuel cells operation: A review, Ceramics International 42(1, Part A) (2016) 35-48.
[8] D. Papurello, S. Silvestri, S. Modena, Biogas trace compounds impact on high-temperature fuel cells short stack performance, International Journal of Hydrogen Energy 46(12) (2021) 8792-8801.
[9] J.F.B. Rasmussen, A. Hagen, The effect of H_2S on the performance of Ni–YSZ anodes in solid oxide fuel cells, Journal of Power Sources 191(2) (2009) 534-541.
[10] J. Mermelstein, M. Millan, N. Brandon, The impact of steam and current density on carbon formation from biomass gasification tar on Ni/YSZ, and Ni/CGO solid oxide fuel cell anodes, Journal of Power Sources 195(6) (2010) 1657-1666.
[11] P.V. Aravind, J.P. Ouweltjes, N. Woudstra, G. Rietveld, Impact of Biomass-Derived Contaminants on SOFCs with Ni/Gadolinia-Doped Ceria Anodes, Electrochemical and Solid-State Letters 11(2) (2008).
[12] P. Fan, X. Zhang, D. Hua, G. Li, Experimental Study of the Carbon Deposition from CH_4 onto the Ni/YSZ Anode of SOFCs, Fuel Cells 16(2) (2016) 235-243.
[13] R. Mücke, N.H. Menzler, H.P. Buchkremer, D. Stöver, Cofiring of Thin Zirconia Films During SOFC Manufacturing, Journal of the American Ceramic Society 92 (2009) S95-S102.
[14] A. Tsoga, A. Naoumidis, D. Stöver, Total electrical conductivity and defect structure of ZrO_2–CeO_2–Y_2O_3–Gd_2O_3 solid solutions, Solid state ionics 135 (2000) 403-409.
[15] A. Varez, E. Garcia-Gonzalez, J. Sanz, Cation miscibility in CeO_2–ZrO_2 oxides with fluorite structure. A combined TEM, SAED and XRD Rietveld analysis, J. Mater. Chem. 16(43) (2006) 4249-4256.
[16] H. Xu, K. Cheng, M. Chen, L. Zhang, K. Brodersen, Y. Du, Interdiffusion between gadolinia doped ceria and yttria stabilized zirconia in solid oxide fuel cells: Experimental investigation and kinetic modeling, Journal of Power Sources 441 (2019).
[17] K. Yang, J.-H. Shen, K.-Y. Yang, I.M. Hung, K.-Z. Fung, M.-C. Wang, Formation of $La_2Zr_2O_7$ or $SrZrO_3$ on cathode-supported solid oxide fuel cells, Journal of Power Sources 159(1) (2006) 63-67.
[18] J. Szász, F. Wankmüller, V. Wilde, H. Störmer, D. Gerthsen, N.H. Menzler, E. Ivers-Tiffée, Nature and Functionality of $La_{0.58}Sr_{0.4}Co_{0.2}Fe_{0.8}O_{3-\delta}$/ $Gd_{0.2}Ce_{0.8}O_{2-\delta}$/ $Y_{0.16}Zr_{0.84}O_{2-\delta}$ Interfaces in SOFCs, Journal of The Electrochemical Society 165(10) (2018) F898-F906.
[19] Z. Lu, S. Darvish, J. Hardy, J. Templeton, J. Stevenson, Y. Zhong, $SrZrO_3$ Formation at the Interlayer/Electrolyte Interface during $(La_{1-x}Sr_x)_{1-\delta}Co_{1-y}Fe_yO_3$ Cathode Sintering, Journal of The Electrochemical Society 164(10) (2017) F3097-F3103.
[20] V. Wilde, H. Störmer, J. Szász, F. Wankmüller, E. Ivers-Tiffée, D. Gerthsen, Effect of $Gd_{0.2}Ce_{0.8}O_2$ Sintering Temperature on Formation of a $SrZrO_3$ Blocking Layer between $Y_{0.16}Zr_{0.84}O_2$, $Gd_{0.2}Ce_{0.8}O_2$ and $La_{0.58}Sr_{0.4}Co_{0.2}Fe_{0.8}O_3$, ECS Transactions 66 (2015) 103-107.
[21] J. Szász, F. Wankmüller, V. Wilde, H. Störmer, D. Gerthsen, N.H. Menzler, E. Ivers-Tiffée, High-Performance Cathode/Electrolyte Interfaces for SOFC, ECS Transactions 68 (2015) 763-771.
[22] C. Lenser, H. Jeong, Y.J. Sohn, N. Russner, O. Guillon, N.H. Menzler, Interaction of a ceria-based anode functional layer with a stabilized zirconia electrolyte: Considerations from a materials perspective, Journal of the American Ceramic Society 101 (2018) 739-748.
[23] T. Horita, N. Sakai, H. Yokokawa, M. Dokiya, T. Kawada, J.v. Herle, K. Sasaki, Ceria-Zirconia Composite Electrolyte for Solid Oxide Fuel Cells, Journal of Electroceramics 1:2 (1997) 155-164.
[24] A. Tsoga, A. Gupta, A. Naoumidis, D. Skarmoutsos, P. Nikolopoulos, Performance of a Double-Layer CGO/YSZ Electrolyte for Solid Oxide Fuel Cells, Ionics 4(3) (1998) 234-240.
[25] A. Tsoga, A. Gupta, A. Naoumidis, P. Nikolopoulos, Gadolinia-doped ceria and yttria stabilized zirconia interfaces: Regarding their application for SOFC technology, Acta Materialia 48 (2000) 4709-4714.
[26] K. Eguchi, N. Akasaka, H. Mitsuyasu, Y. Nonaka, Process of solid state reaction between doped ceria and zirconia Solid State Ionics 135 (2000) 589-594.
[27] P.-L. Chen, I.-W. Chen, Grain growth in CeO_2: dopant effects, defect mechanism, and solute drag, Journal of the American Ceramic Society 79 (1996) 1793-8000.

[28] M. Schönleber, D. Klotz, E. Ivers-Tiffée, A Method for Improving the Robustness of linear Kramers-Kronig Validity Tests, Electrochimica Acta 131 (2014) 20-27.
[29] T. van Dijk, A.J. Burggraaf, Grain boundary effects on ionic conductivity in ceramic $Gd_xZr_{1-x}O_{2-(x/2)}$ solid solutions, Physica Status Solidi (a) 63(1) (1981) 229-240.
[30] N.M. Beekmans, L. Heyne, Correlation between impedance, microstructure and composition of calcia-stabilized zirconia, Electrochimica Acta 21(4) (1976) 303-310.
[31] J. Schindelin, I. Arganda-Carreras, E. Frise, V. Kaynig, M. Longair, T. Pietzsch, S. Preibisch, C. Rueden, S. Saalfeld, B. Schmid, J.Y. Tinevez, D.J. White, V. Hartenstein, K. Eliceiri, P. Tomancak, A. Cardona, Fiji: an open-source platform for biological-image analysis, Nat Methods 9(7) (2012) 676-82.
[32] A. Tsoga *et al.*, Microstructure and interdiffusion phenomena in YSZ-CGO composite electrolyte, Materials science forum 308 (1999).
[33] E. Tani, M. Yoshimura, S. Somiya, Revised Phase Diagram of the System ZrO_2-CeO_2 below 1400°C, Journal of the American Ceramic Society 66(7) (1983) 506-510.
[34] M. Price, J. Dong, X. Gu, S.A. Speakman, E.A. Payzant, T.M. Nenoff, Formation of YSZ-SDC Solid Solution in a Nanocrystalline Heterophase System and Its Effect on the Electrical Conductivity, Journal of the American Ceramic Society 88(7) (2005) 1812-1818.
[35] J. Luo, R.J. Ball, R. Stevens, Gadolinia doped ceria/yttria stabilised zirconia electrolytes for solid oxide fuel cell applications, 39 (2004) 235– 240.
[36] V. Rührup, H.-D. Wiemhöfer, Ionic Conductivity of Gd- and Y-Doped Ceria-Zirconia Solid Solutions, Z. Naturforsch. 61b (2006) 916-922.
[37] A. Arabaci, Effect of Sm and Gd dopants on structural characeristics and ionic conductivity of ceria Ceramics International 41 (2015) 5836-5842.
[38] S. Kuharuangrong, Ionic conductivity of Sm, Gd, Dy and Er-doped ceria, Journal of Power Sources 171(2) (2007) 506-510.
[39] G.E. Lloyd, Atomic number and crystallographic contrast images with the SEM: a review of backscattered electron techniques, Mineralogical Magazine 51(359) (1987) 3-19.
[40] F. Wankmüller, J. Szász, J. Joos, V. Wilde, H. Störmer, D. Gerthsen, E. Ivers-Tiffée, Correlative tomography at the cathode/electrolyte interfaces of solid oxide fuel cells, Journal of Power Sources 360 (2017) 399-408.
[41] M. Ozawa, K. Imura, Cation Diffusion at Interface between Y_2O_3 Stabilized ZrO_2 and CeO_2., Journal of the Japan Society of Powder and Powder Metallurgy 65(4) (2018) 187-190.
[42] S. A. Acharya, V.M. Gaikwad, S.W. D'Souza, S.R. Barman, Gd/Sm dopant-modified oxidation state and defect generation in nano-ceria, Solid State Ionics 260 (2014) 21-29.
[43] A. Nenning, C. Bischof, J. Fleig, M. Bram, A.K. Opitz, The Relation of Microstructure, Materials Properties and Impedance of SOFC Electrodes: A Case Study of Ni/GDC Anodes, Energies 13(4) (2020).
[44] J. Szász, F. Wankmüller, J. Joos, V. Wilde, H. Störmer, D. Gerthsen, E. Ivers-Tiffée, Correlating Cathode/Electrolyte Interface Characteristics to SOFC Performance, ECS Transactions 77 (2017) 27-34.
[45] J.D. Vero, K. Develos-Bagarinao, D.H. Cho, H. Kishimoto, K. Yamaji, H. Yokokawa, Effect of LSCF Microstructure on GDC Interlayer Stability and Cation Diffusion in Porous and Dense LSCF/GDC/YSZ Triplets, ECS Transactions 68(1) (2015) 1943-1953.
[46] R. M. Batista, E.N.S. Muccillo, Densification and grain growth of 8YSZ containing NiO, Ceramics International 37(3) (2011) 1047-1053.
[47] C.-Y. Chen, Y.-R. Lyu, Effect of NiO addition on properties of bulk yttria-doped ceria sintered from their spray pyrolyzed powder, Ceramics International 38(4) (2012) 3291-3300.
[48] D. Xu, K. Li, Y. Zhou, Y. Gao, D. Yan, S. Xu, The effect of NiO addition on the grain boundary behavior and electrochemical performance of Gd-doped ceria solid electrolyte under different sintering conditions, Journal of the European Ceramic Society 37(1) (2017) 419-425.
[49] F. Ye, T. Mori, D.R. Ou, J. Zou, J. Drennan, S. Nakayama, M. Miyayama, Effect of nickel diffusion on the microstructure of Gd-doped ceria (GDC) electrolyte film supported by Ni–GDC cermet anode, Solid State Ionics 181(13-14) (2010) 646-652.
[50] S. Nikodemski, J. Tong, R. O'Hayre, Solid-state reactive sintering mechanism for proton conducting ceramics, Solid State Ionics 253 (2013) 201-210.

[51] K.-R. Lee, C.-J. Tseng, S.-C. Jang, J.-C. Lin, K.-W. Wang, J.-K. Chang, T.-C. Chen, S.-W. Lee, Fabrication of anode-supported thin BCZY electrolyte protonic fuel cells using NiO sintering aid, International Journal of Hydrogen Energy 44(42) (2019) 23784-23792.
[52] Y. Huang, R. Merkle, J. Maier, Effects of NiO addition on sintering and proton uptake of $Ba(Zr,Ce,Y)O_{3-\delta}$, Journal of Materials Chemistry A 9(26) (2021) 14775-14785.